Mon. Not. R. Astron. Soc. **376,** 113–124 (2007) doi:10.1111/j.1365-2966.2006.11296.x

Smooth Particle Lensing

Dominique Aubert,[1⋆] Adam Amara[1⋆] and R. Benton Metcalf[2]

[1]*Service d'Astrophysique, CEA Saclay, Gif sur Yvette 91191, France*
[2]*Max Planck Institute for Astrophysics, Garching 8574, Germany*

Accepted 2006 November 15. Received 2006 September 5; in original form 2006 April 13

ABSTRACT

We present a numerical technique to compute the gravitational lensing induced by simulated haloes. It relies on a 2D-Tree domain decomposition in the lens plane combined with a description of *N*-body particles as extended clouds with a non-singular density. This technique is made fully adaptive by the use of a density-dependent smoothing which allows one to probe the lensing properties of haloes from the densest regions in the centre or in substructures to the low-density regions in the outskirts. 'Smooth Particle Lensing' (SPL) has some promising features. First, the deflection potential, the deflection angles, the convergence and the shear are direct and separate end-products of the SPL calculation and can be computed at an arbitrary distribution of points on the lens plane. Secondly, this flexibility avoids the use of interpolation or a finite differentiation procedure on a grid, does not require padding the region with zeros and focuses the computing power on relevant regions. The SPL algorithm is tested by populating isothermal spheres and ellipsoids with particles and then comparing the lensing calculations to the classical fast Fourier transform based technique and analytic solutions. We assess issues related to the resolution of the lensing code and the limitations set by the simulations themselves. We conclude by discussing how SPL can be used to predict the impact of substructures on strong lensing and how it can be generalized to weak-lensing and cosmic shear simulations.

Key words: gravitational lensing – methods: *N*-body simulations – methods: numerical.

1 INTRODUCTION

The concordance model of cosmology has now been widely accepted as it is in agreement with an extensive range of observational probes (Bahcall et al. 1999; Wang et al. 2000; Spergel et al. 2003; Van Waerbeke & Mellier 2003). One of the central ingredient to the model is cold dark matter (CDM). However, in order to draw detailed comparison between theoretical models of CDM and the observed Universe, high-resolution computational simulations are required. The simplest simulations calculate the evolution of density perturbations in a Universe, where the matter contribution is composed entirely of CDM particles (Navarro, Frenk & White 1996; Moore et al. 1998; Evrard & Virgo Collaboration 1999; Bode & Ostriker 2003). The density distributions that these simulations produce cover a wide range of scales, with an enormous wealth of information. The challenge that we face now is finding ways to efficiently mine this data and compare it to observational probes.

Compact collapsed objects, such as galaxies, groups and clusters, have been studied extensively in the simulations. In doing so, a discrepancy known as 'the substructure problem' has been identified (Klypin et al. 1999; Moore et al. 1999; Weller et al. 2005), where the number of small scale objects formed in simulated Milky Way's haloes is significantly greater than the number of observed satellites. There is some ambiguity as to how dwarf galaxies are matched with subhaloes of a given mass (see e.g. Stoehr et al. 2002; Kazantzidis et al. 2004). It is perhaps possible to resolve the problem for some mass range by adjusting this relation, but it is always the case that the simulations predict more subhaloes than observed in dwarf galaxies. Whether this is a result of suppressed star formation in small haloes or a deeper problem with the CDM model is not yet clear.

The flux ratios between images in strong gravitational lenses are powerful tools for studying substructure even when it is not associated with any observable stars or gas (Mao & Schneider 1998; Metcalf & Madau 2001; Chiba 2002; Dalal & Kochanek 2002; Metcalf & Zhao 2002; Moustakas & Metcalf 2003; Metcalf et al. 2004). A number of authors have investigated the implications of *N*-body results on strong lensing. One approach is to divide the study into two steps. The first step is to study the statistical properties of *N*-body halo, such as the radial distribution of substructure. The second step is to predict the lensing implications separately by using analytic calculations (Mao et al. 2004). This method has a number of drawbacks. For instance, they are dependent on the selection criteria used to identify substructures, and analytic models for substructure lensing do not incorporate all the necessary effects.

⋆E-mail: dominique.aubert@cea.fr (DA); aamara@cea.fr (AA)

Another approach has been to study the lensing properties of the simulations directly using ray-shooting. This approach also suffers from a number of drawbacks, which we will investigate here.

Both of these methods are limited by the resolutions of the *N*-body simulations. First, there is a mass resolution, set by the fact that haloes are modelled using a finite number of particles. The current generation of simulations typically provide dark matter haloes with 1–10 million particles within the virial radius. For a Milky Way-sized galaxy, this corresponds to a mass resolution of 10^5–10^6 $M_\odot$. Any results below this mass-scale can only be reached by extending what we see for larger mass-scales (Mao et al. 2004). Numerical simulations are also limited in spatial length-scales. The current generation of simulations have a spatial resolution of 50–500 pc for a galaxy-sized halo. Although these scales result from an astonishing dynamic range for cosmological simulations, they still place major constraints on the strong-lensing studies since strong lensing probes the very inner regions of galaxies, typically radii of 1–10 kpc, .

Probing these inner regions in detail is also limited by the fact that the baryonic component of the galaxy plays an important role. An ideal simulation would include dark matter as well as the gas, stars and their complex interactions. Strong-lensing studies of such simulations have been performed (Bradač et al. 2004). However, it is well-known that the current generation of simulations that contain baryons struggle to reproduce realistic galaxies (see e.g. Navarro, Frenk & White 1995; Navarro & Steinmetz 1997). An alternative approach is to take the results of an *N*-body dark matter simulation and add a model for a realistic galaxy and then allow the dark matter to relax in the new potential (Amara et al. 2006). Although somewhat ad hoc, this approach allows us to decouple the contributions due to observed baryonic distributions from those due to the dark matter in their haloes.

A final limitation of directly studying the strong lensing of *N*-body haloes is the technique used to perform the ray shooting. Various methods were proposed by several authors (see e.g. Wambsganss, Cen & Ostriker 1998; Meneghetti et al. 2000) and among them, a popular method for calculating the lensing properties of object is to project it on to a 2D grid and to calculate the gravitational potential using a fast Fourier transform (FFT) technique (see e.g. Bradac et al. 2002; Amara et al. 2006). This method has the advantage of being significantly faster to compute than others, scaling as $N \log N$ and not N^2 as in the case of particle–particle calculations. The FFT method, however, does suffer from two major drawbacks. The first is that the resolution of the lensing calculation is limited to grid size on which the FFT is performed, and the second is that using FFT routines introduces repeating boundary conditions into the problem. The latter means that the galaxy being studied is no longer an isolated object (see Fig. 1). It becomes a part of an endless 2D lattice of identical galaxies. The impact of this lattice of external galaxies can be controlled by adding a buffer of zeros around the galaxy being studied. However, adding a large buffer compounds the resolution problem, since for a fixed grid size ($N \times N$) the number of grid points that cover the galaxy is reduced. Finding the right amount of buffering that will balance between these two opposing requirements is not a straightforward exercise. Even when the right amount of buffering is found, evaluating the impact of these constraints on lensing results is not trivial. The memory-consuming strategy of zero-padding can be avoided following a method described by Puchwein et al. (2005): the effect of boundary conditions is corrected by removing the periodical signal induced by a 2D lattice of points (minus the one located at the halo's centre) with the same mass as the halo. For a given amount of memory, a larger fraction of the lens plane is then unaffected by periodic artefacts. However, the gain in memory efficiency is not complete: a fraction of the lens plane remains affected by periodic artefacts (the external region of the halo) because the orders higher than the monopole of the mass's distribution are not used for the correction.

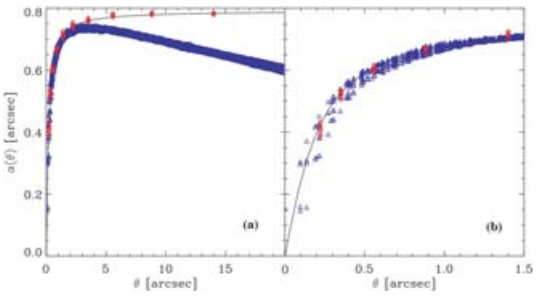

Figure 1. Comparison of the deflection angles calculated using the FFT method (blue triangles) and SPL method (red diamonds) with the analytic prediction (black curve). On the left-hand side [panel (a)], we see that for large radii the FFT method becomes dominated by the repeating boundary conditions. This is a problem that does not occur using the SPL method. However, we know that the strong-lensing region is very close to the centre. On the right-hand side [panel (b)], we see that the problem of repeated boundary conditions is less pronounced. Here a buffering of one-quarter is used, i.e. one-quarter of the FFT length is filled with zeros.

In this paper, we discuss an alternative method for performing the lensing calculations needed for ray-shooting. We focus on the methodology and postpone the applications to a forthcoming paper. This technique combines a smooth description of particles with well-defined lensing properties and a tree-based domain decomposition. First, we describe the principle of ray shooting through an FFT and the so-called 'Smooth Particle Lensing' (hereafter SPL) technique. Resolution effects and the capacities of SPL are then investigated using realizations of analytic models, such as softened isothermal spheres and ellipsoids. Finally, we conclude by discussing the intrinsic limitations induced by simulations regarding lensing predictions and present the future applications of the SPL technique.

2 RAY SHOOTING

To calculate the lensing properties of an object, we first adopt the thin lens approximation in which the mass distribution is collapsed to a plane perpendicular to the line of sight, the lens plane. Light is then assumed to travel along straight lines between the source, lens plane and the observer. Rays experience a discrete deflection at the lensing plane. The deflection angle can be calculated directly from the mass distribution. This is an excellent approximation for galaxy and galaxy cluster size lenses.

2.1 Lensing formalism

The deflection angle $\boldsymbol{\alpha}$ of a lens can be calculated from deflection potential, $\psi(\boldsymbol{\theta})$, of the mass distribution:

$$\boldsymbol{\alpha}(\boldsymbol{\theta}) = \nabla\psi(\boldsymbol{\theta}). \tag{1}$$

This deflection potential is simply twice the 2D Newtonian surface potential and can be calculated from the convergence, $\kappa(\boldsymbol{\theta})$:

$$\nabla^2\psi(\boldsymbol{\theta}) = 2\kappa(\boldsymbol{\theta}). \tag{2}$$

The convergence is a dimensionless quantity that can be calculated from the surface mass distribution on the lensing plane, $\Sigma(\boldsymbol{\theta})$, and

geometric factors:

$$\kappa(\boldsymbol{\theta}) = \frac{D_{\rm L} D_{\rm LS}}{D_{\rm S}} \frac{4\pi G}{c^2} \Sigma(\boldsymbol{\theta}) = \frac{\Sigma(\boldsymbol{\theta})}{\Sigma_{\rm c}}, \tag{3}$$

where $D_{\rm L}$ is the angular diameter distance from the observer to the lens, $D_{\rm LS}$ is the angular diameter distance from the lens to the source, and $D_{\rm S}$ is the angular diameter distance between the observer and the source. These factors are usually collected together into a term known as the critical density, $\Sigma_{\rm c} = c^2 D_S / 4\pi G D_{\rm L} D_{\rm LS}$. When the surface density of a lens is greater than half the critical density, that is, $\kappa > 1/2$, a single source can have multiple images. Mapping a position on the lensing plane, $\boldsymbol{\theta}$, to the position of the source, $\boldsymbol{\beta}$, is done through the lens equation:

$$\boldsymbol{\beta}(\boldsymbol{\theta}) = \boldsymbol{\theta} - \boldsymbol{\alpha}(\boldsymbol{\theta}). \tag{4}$$

The other properties of a gravitationally lensed system, such as the magnification and the shear, can be calculated using the distortion matrix, $A_{ij} \equiv \frac{\partial \beta^i}{\partial \theta^j}$. Magnification is then given by $\mu(\boldsymbol{\theta}) = |A|^{-1}$, that is:

$$\mu(\boldsymbol{\theta}) = \frac{1}{[1 - \kappa(\boldsymbol{\theta})]^2 - |\gamma(\boldsymbol{\theta})|^2}, \tag{5}$$

and the two components of shear are defined as $\gamma_1 = (A_{11} - A_{22})/2$ and $\gamma_2 = A_{12} = A_{21}$.

In the following sections, we first describe the classical method based on the Fourier transforms to compute the lensing potential of simulated haloes. We then introduce the 'SPL' technique.

2.2 Fast Fourier transform

Solving the Poisson equation (2), can be performed in Fourier space, where the equation becomes $\ell^2 \tilde{\psi}(\ell) = \tilde{\kappa}(\ell)$, where ℓ stands for the Fourier wavenumber. This allows us to use FFTs which use a grid-based method for finding the Fourier transform of a field. The first step is to put the particles on to a 2D grid. Here, we do this using a Cloud In Cell (CIC) routine. At this stage the first undesirable effect of the FFT method is introduced. Placing the particles on a grid using CIC introduces a global smoothing with an effective CIC window function and limits the points where the lensing properties are calculated. The CIC smoothing is a nuisance in strong lensing because this scale does not necessary correspond to scale that is significant to the investigation and so makes the interpretation of the results more difficult. It should also be noted that using the FFT method for ray shooting is also widely used in weak-lensing and cosmic shear simulations. In these regimes the CIC smoothing is also problematic. When considering the weak-lensing regime, one is typically interested in the auto-correlations of the lensing field. For such an analysis, great care must be taken since it is widely known that using a simple FFT method to solve the Poisson can result in a loss of power on small scales due the CIC smoothing. This loss of power affects on large scales since the CIC window function is extended in a Fourier space. This effect is well known and can be corrected for (Smith et al. 2003); however, it is not clear in the literature if this correction is always applied. In the strong-lensing regime where the correlation function is usually not under investigation, this loss of power may be less problematic, but the global smoothing is still, nevertheless, undesirable. More problematic in the strong-lensing case is the fact the lensing calculations are performed on a grid.

When studying the strong-lensing properties of an isolated halo, we are particularly interested in the properties of the mass distribution in the very central regions of the halo since the impact parameters for light rays are typically small. At the same time, it is important to account for the distribution of mass outside this central region since it will also have an impact on the lensing signal. This means that the entire galaxy must be placed on to a grid and the lensing properties calculated at each grid point. However, while locating and analysing images, only the central ∼0.1 per cent of the grid points are ever used. This means that although the FFT is the fastest known method for computing the lensing properties at the N grid points, the fact that most of these points are not used becomes a significant loss of efficiency. Restricting calculation results to grid points is also undesirable, since, in order to study multiply imaged systems, interpolation between the grid points cannot be avoided as it is highly unlikely that all images will sit on grid points. On small scales, the ideal lensing solver would therefore be able to evaluate the lensing properties of a mass distribution at an arbitrary point.

For N-body simulations, the underlying density distribution is represented by point masses. A first limiting scale appears, which corresponds to the force resolution of the original N-body simulation. This is because density variation on smaller scales cannot be trusted to be of real significance. Furthermore, without any additional smoothing, the shot noise from these point sources would dominate over the signals investigated and a flexible smoothing appears to be central to a lensing solving method. The optimal smoothing scale required to reduce shot-noise is expected to be linked to the local number density of particles, which is difficult to achieve with a fixed-grid method.

On large scales, the FFT method also suffers drawbacks. The introduction of repeating boundary condition has already been discussed. The adverse effect of this for strong-lensing studies is that a buffer needs to be placed around the galaxy halo. Since the resolution limit is set by the maximum array that can be manipulated by a CPU, loading this array with zeros has a detrimental effect on resolution. Once again, the impact of introducing repeating boundary conditions on weak lensing and cosmic shear needs to be considered carefully since this will impact correlations on large scales. It is possible to construct a grid-based method that does not introduce a repeating boundary condition; however, it complicates the calculation and these methods are not implemented in the current generation of ray shooting routines.

2.3 Smooth Particle Lensing

Not all lensing calculations in numerical simulations use Fourier transforms; for example, the method used by Wambsganss et al. (1998) involves a tree-based method to calculate deflection angles. Here, we suggest to go beyond such a calculation in order to compute all the lens quantities while using an adaptive description of particles.

The 'SPL' technique is based on the discrete description of haloes in N-body simulation and relies on the fact that each particle will contribute to the projected potential measured at a given point. If i labels the ith particle of a simulated halo, the 2D deflection potential measured at $\boldsymbol{r}$ is given by

$$\phi(\boldsymbol{r}) = \sum_i \phi_i(\boldsymbol{r}), \tag{6}$$

where $\phi_i(\boldsymbol{r})$ is the potential created by a single particle. Any linear function of the potential can also be expressed as a sum over particles. The deflection angle is written as

$$\boldsymbol{\alpha}(\boldsymbol{r}) = \nabla\phi(\boldsymbol{r}) = \sum_i \nabla\phi_i(\boldsymbol{r}) = \sum_i \boldsymbol{\alpha}_i(\boldsymbol{r}), \tag{7}$$

where $\boldsymbol{\alpha}_i(\boldsymbol{r})$ are the 2D deflection angles produced by a single particle. Likewise the convergence κ and the shear γ are

$$\kappa(\boldsymbol{r}) = \sum_i \kappa_i(\boldsymbol{r}) \tag{8}$$

and

$$\gamma(\boldsymbol{r}) = \sum_i \gamma_i(\boldsymbol{r}), \tag{9}$$

respectively. Therefore, it is possible to derive the lensing properties of an arbitrary distribution of points by summing the contribution of individual particles. However, we are left with two difficulties at this stage. First, we have to find a convenient single-particle lens model, with a 'clean' behaviour from both a physical and numerical point of view. Secondly, we have to find an efficient way to perform the sums described in equations (6), (7), (8) and (9). These two difficulties are assessed in the next two Sections.

2.3.1 *Smoothed particles*

A natural way to describe the particles would be to describe their density as Dirac's $\delta(\boldsymbol{r})$ functions, leading to 2D potential $\phi(\boldsymbol{r}) \sim \log(r)$ and deflection angles $|\boldsymbol{\alpha}(\boldsymbol{r})| \sim 1/r$. Not only such a choice would induce a noisy projected density but it creates singularities in the deflection angles, when close encounters between a ray and a particle occur. Another choice would be to smooth the force applied to rays by the particles, for example, by assuming $|\boldsymbol{\alpha}(\boldsymbol{r})| \sim 1/\sqrt{r^2+\epsilon^2}$. It would correspond to the procedure applied in *N*-body calculations. However, it still leads to singular convergence and shear for a single particle, making the method less powerful than it can be. Hence, we decided to start from a given functional form of a single particle density profile (i.e. its convergence κ), to construct its potential back by solving the Poisson equation, leading to expressions for the single-particle deflection angles and shear.

Let us consider a particle with a mass m_p and a lens configuration where the deflector's redshift is z_L and the corresponding critical density Σ_c. Positions on the lens plane are given in terms of *physical* radii r while angles can be recovered by

$$\theta = \frac{r}{D_\mathrm{L}(z_\mathrm{L})}, \tag{10}$$

where $D_\mathrm{L}(z_\mathrm{L})$ stands for the angular diameter distance of the lens. We chose to model the single-particle projected density by a 2D isotropic 'Gaussian' function (see also Fig. 2). The related convergence is given by

$$\kappa(r) = \frac{m_\mathrm{p}}{2\pi\sigma^2\Sigma_\mathrm{c}} \exp\left(-\frac{r^2}{2\sigma^2}\right), \tag{11}$$

where r stands for the distance between the ray and the particle. The corresponding potential is given by

$$\phi(r) = \frac{m_\mathrm{p}}{4\pi\Sigma_\mathrm{c}} \left[\log\left(\frac{r^4}{4\sigma^4}\right) - 2\mathrm{Ei}\left(-\frac{r^2}{2\sigma^2}\right)\right], \tag{12}$$

where $\mathrm{Ei}(x) = -\int_x^\infty \exp(-x)/x \, \mathrm{d}x$. The deflection angle is given by

$$\alpha(r) = m_\mathrm{p} \frac{\mathrm{e}^{-(r^2/2\sigma^2)} - 1}{\pi r \Sigma_\mathrm{c}}. \tag{13}$$

One can see in Fig. 2 that the deflection angles (or equivalently the force applied to the ray by the particle) has a 'hollow' behaviour because of the finite but non-nil extension of the particle: the force rises as the ray gets closer to the 'border' (typically $r \sim 3\sigma$) of the particle then it adopts a behaviour in $1/r$ as expected. The associated shear created by a single particle is given by

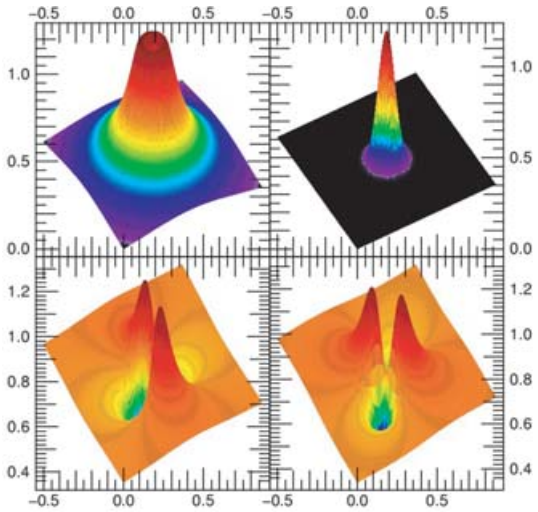

Figure 2. The properties of each of the particles in the simulation. Each particle has a 2D Gaussian surface density distribution. The top left-hand panel shows the 2D gravitational deflection angle (α); the top right-hand panel shows the convergence (κ) and the bottom left-hand and right-hand panels show the two components of shear (γ_1 and γ_2).

$$\gamma_1(x, y) = \kappa(r)\frac{(x^2 - y^2)}{r^4}\Gamma(r, \sigma) \tag{14}$$

and

$$\gamma_2(x, y) = 2\kappa(r)\frac{xy}{r^4}\Gamma(r, \sigma), \tag{15}$$

where

$$\Gamma(r, \sigma) = r^2 + 2[1 - \mathrm{e}(r^2/2\sigma^2)]\sigma^2. \tag{16}$$

The σ parameter acts as a smoothing parameter and as $\sigma \to 0$, the single particle density profile tends to a Dirac-$\delta(r)$ function. This smoothing parameter can be a simple constant over all the particles, or in a more sophisticated way a function of the considered particle or ray. We show in Section 3 how this choice can affect the final results.

2.3.2 *Tree 2D*

The single-particle model being set, an efficient way to perform the sums over all the particles' contributions remains to be found. Evidently, it cannot be performed by direct summation, since the CPU consumption would scale as $N_\mathrm{rays} \times N_\mathrm{part}$. Furthermore, an improvement in the simulation resolution, i.e. in N_part, would strongly affect the computation time, while we want the simulation's resolution to be an advantage and not a limitation. For these reasons, we suggest to use a summation technique based on a tree-based domain decomposition. These techniques have been widely used in numerical simulations to compute the 3D force created by an arbitrary distribution of particles (e.g. Barnes & Hut 1986; Bouchet & Hernquist 1988; Dikaiakos & Stadel 1996; Bertschinger 1998). They are known to scale in a logarithmic way, that is, they scale as $N_\mathrm{rays} \times \log N_\mathrm{part}$ in the current case. Here, we apply the 2D version of this algorithm to compute all the lensing quantities created by a set of particles distributed within the lens plane. Most of the following have been strongly inspired by the description made by Dikaiakos & Stadel (1996) for the *N*-body code PKDGRAV.

The particles' distribution is organized following a 2D version of KD-Tree structures (see e.g. Moore 1991) or 2D-Tree. First, the space is divided in two subregions that contain the same number of particles. The whole box (or 'the root') is connected to two 'branches', which correspond to these two subregions. The same 'space-splitting' procedure is then applied to these smaller regions (or 'cells'), adding a new level to the tree with four new branches. In the end, the recursive application of this procedure leads to a binary tree, with final branches (or 'leaves') containing $N_{\rm leaves}$ particles. We chose $N_{\rm leaves} = 8$. While building the tree, each cell is being assigned an opening radius given by

$$r_{\rm open} = \frac{2r_{\rm com}}{\theta_{\rm Tree}\sqrt{3}} + r_{\rm centre}. \quad (17)$$

The quantities $r_{\rm com}$ and $r_{\rm centre}$ stand for the maximal possible distance between a particle inside the cell and, respectively, its centre of mass and its geometrical centre. The free parameter $\theta_{\rm Tree}$ controls the opening radius, as explained below.

The lensing computation is performed by walking down the tree. We discuss this walking procedure for the computation of the force felt by a ray (or equivalently the deflection angles $\boldsymbol{\alpha}$) but it translates to the κ and γ computation. Let us consider the force felt by a ray at the point $\boldsymbol{P}$ on the lens plane. A given cell is opened if the distance r_P between its centre of mass and $\boldsymbol{P}$ satisfies $r_{\boldsymbol{P}} < r_{\rm open}$. If the criterion is satisfied, the same test is performed on the two branches connected to the current cell. This recursion can be stopped in two manners. First, the current cell is a leaf : the force felt by $\boldsymbol{P}$ is obtained by adding the forces created by each particle of this cell. Second possibility is when the distance r_P between its centre of mass and $\boldsymbol{P}$ satisfies the relation $r_{\boldsymbol{P}} > r_{\rm open}$: the force felt by $\boldsymbol{P}$ is obtained by computing the force applied by the whole cell, assuming a monopole with a mass equal to the number of particles inside the cell and centred on its centre of mass. In other words, the effect of distant cells is modelled as the effect of a macroparticle with the same properties as a single one but scaled to the correct mass.

The parameter $\theta_{\rm Tree}$ appears as a performance control parameter. In equation (17), a small $\theta_{\rm Tree}$ implies that all the cells are likely to be opened. In this case, the force computation is close to the direct summation of the interactions created by all the particles, resulting in slow computations. Conversely, a large $\theta_{\rm Tree}$ would speed up the procedure but would also lower the accuracy of the computation.

At this stage, we end up with two free parameters: $\theta_{\rm Tree}$ which controls the overall summation performance and σ which introduces a finite spatial resolution. In the following, we mostly choose $\theta_{\rm Tree} = 0.7$: it led to accurate results while ensuring a good performance of the summation (see also 3.1.3). The influence of σ is more complex to establish and at the heart of the lensing computation at high resolution.

2.3.3 Adaptive smoothing

The final step to the SPL's setting is the implementation of an adaptive smoothing. It is clear that if particles sample the projected density, their 'extension' should be density-dependent. A constant smoothing length may result in oversmoothing in high-density regions, while it would induce shooting noise in low-density environment (see also Section 3.1). Hence, σ should be a function of the local density of particles. Two strategies are possible, the first being that each dark matter particle is assigned a σ by computing its local density. In practice, this involves the computation of the local density for 10^6–10^7 particles, which can be highly CPU consuming. The second strategy consists of assigning the *same* σ to all the particles while its value depends on the local density of particles at the position of the light ray. For different light rays σ changes. This physically makes sense since the density should be correctly estimated at the location of the light rays, not at the dark matter particles' locations. Because the number of light rays can be much smaller than the typical number of particles, this strategy significantly improves the computational efficiency. It naturally implies that particles distant to the current ray have inappropriate σ. However, they only contribute to the deflection angle and, being distant, their influence varies as $m_{\rm p}/r$ independently of σ; no loss of accuracy can be detected. We decide to adopt this second strategy based on the density at the light rays' positions.

In our implementation, we chose to estimate this density by computing the distance $r_{\rm sph}$ to the $N_{\rm sph}$th closest particle to the ray. In practice, this computation is made while walking the tree during the lensing computation. The density is simply estimated by

$$\rho_{\rm ray} = \frac{N_{\rm sph}}{\pi r_{\rm sph}^2}. \quad (18)$$

This procedure is equivalent to an SPH-density estimation with a top-hat kernel. Even though more complex kernels may be used (see e.g. Li et al. 2006), this simple choice is sufficient. Finally, we set a smoothing length for a given ray by applying the following relation:

$$\sigma = \sqrt{\frac{N_\sigma}{\pi\rho_{\rm ray}}}. \quad (19)$$

The N_σ parameter controls the smoothing strength and appears as a number of particles over which the smoothing is applied. Typically, we found that $N_\sigma \sim 64$–256 gives good results.

2.3.4 SPL features

Having described the technical aspects of SPL, we discuss briefly the interesting features of the method. First, a whole set of lensing quantities (ψ, $\boldsymbol{\alpha}$, κ and γ) are directly computed from the particles' distribution and this can be extended to any linear function of the potential. Secondly, a key aspect of SPL is its flexibility in terms of geometry. No grid or any a priori geometry is required for the sampling of the projected density. This method takes full advantage of the sampling performed by the simulation itself. At any point on the lens plane, we simply sum up all the particles' contribution to any lensing quantity. This eliminates the use of interpolation procedures, which do not provide additional information compared to a coarser sampling. Furthermore, the computing power can be focused on an arbitrary region with any geometry. The result is an insensitivity of SPL to periodic artefacts, preventing the loss of computational power and memory (see also Fig. 1). For instance, caustics can be mapped back by computing the deflections angle only along the critical curves. Also image distortions can be investigated at very high resolution by focusing the SPL calculation around an image spotted at lower resolution.

These features arise from the decoupling in SPL between the lens sampling and the computation of the lens' effect on the light rays. In N-body calculations, the relevant quantity is the force exerted by particles on particles. Therefore, it makes sense to compute the forces at points where the density is sampled. In gravitational lensing, the relevant calculation is the influence of particles on light rays. Hence, we are not forced to map the lensing quantities on a regular grid or at the particle positions. Grid-based methods do not achieve this decoupling easily, while it is natural for tree-based methods.

This makes tree-based (or more generally summation-based) methods much more appropriate to perform the computations, compared to *N*-body calculations, where the pros and cons of grid-based and tree-based techniques can still be debated.

3 TESTS USING ANALYTIC DISTRIBUTIONS

3.1 Non-Singular Isothermal Sphere

3.1.1 Model

To test the impacts of finite resolution, it is important to compare our measured lensing properties with analytic expectations. For our initial test, we focus on radially symmetric case. We begin by defining a convergence field from a Non-Singular Isothermal Sphere (NSIS):

$$\kappa(\theta) = \frac{\kappa_o}{\sqrt{\theta^2 + \theta_o^2}}. \tag{20}$$

Throughout this paper, we scale this distribution to be consistent with a halo of mass, $M_{\rm h} = 1 \times 10^{13}\,{\rm M}_\odot$, within a radius, $r_{\rm h} = 0.5$ Mpc. The halo is then assumed to be at a redshift of $z = 0.8$ and the background sources are assumed to be at a redshift of $z = 3.0$.

Solving the Poisson equation (2) for the convergence field described earlier leads to the lensing potential:

$$\psi(\theta) = 2\theta_o\kappa_o \left[\sqrt{1 + \frac{\theta^2}{\theta_o^2}} - \log\left(1 + \sqrt{1 + \frac{\theta^2}{\theta_o^2}}\right)\right]. \tag{21}$$

and a deflection field of

$$\alpha(\theta) = 2\kappa_o \frac{\theta_o}{\theta}\left(\sqrt{1 + \frac{\theta^2}{\theta_o^2}} - 1\right). \tag{22}$$

The subsequent shear and magnification are simply calculated from this deflection angle by constructing the distortion matrix, $\mathbf{A}_{ij}$ and using the definition of equation (5).

In order to draw conclusions about current numerical simulations, we chose to study an NSIS where the core radius is 2000 times smaller than a typical virial radius for a galaxy of mass M. In our case, M is $10^{13}\,{\rm M}_\odot$. This core radius was chosen because it is approximately the smoothing scale expected in current *N*-body simulations. These simulations contain roughly 10^7 particles. To accurately simulate an NSIS of this type under these conditions, we first converted the density distribution into a probability distribution function. We then randomly sampled this distribution 10^7 times to obtain positions for the particles. Finally by setting the mass of each of these points to $10^6\,{\rm M}_\odot$, we were able to produce a realization of our NSIS with particle sampling similar to that of an *N*-body halo. Fig. 3 shows the cumulative mass profile for two NSIS haloes sampled with 10^7 and 10^6 particles. For both models, the mass profile is reproduced at the per cent level or less for radii greater than the core radius ($r_{\rm c} = 0.037$ arcsec in our lens configuration). This agreement suggests that any departure or scatter at a greater level around the theoretical profiles is unlikely to be related to the finite number of particles. A larger departure ($\sim$10 per cent) to the theoretical profile is found for the million-particle halo for $r \sim 0.01$ arcsec: we avoid such regions in the following investigations that use this simulated model.

3.1.2 Radial profiles

As an illustration, we begin by testing the impact of smoothing scale with a *constant* smoothing scale σ. We do this by calculating the inverse magnification for a number of rays which are placed on concentric rings around the centre of the NSIS. Such a test is crucial since magnification(being a combination of second-order derivatives of the lensing potential) is the quantity that is most sensitive to variations in density. Furthermore, magnification serves to spot the location of critical lines and caustics. The radii of the rings are chosen so that they are distributed evenly in $\log(\theta)$ which allows us to cover a wide range of scales and hence take full advantage of the sampling flexibility of the SPL method.

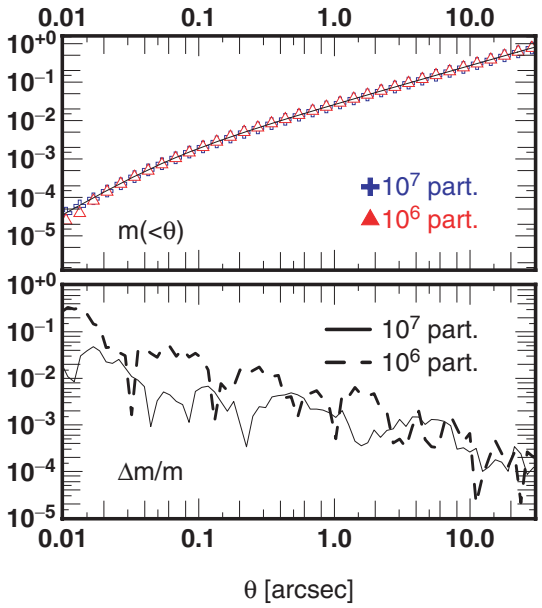

Figure 3. Top panel: the cumulative mass profile of the NSIS model sampled with 10^7 particles (blue crosses) and 10^6 particles (red triangles). The core radius, $r_{\rm h}/2000$, corresponds to 0.037 arcsec in our template lens configuration. The solid line stands for the theoretical profile. Bottom panel: the residual error on the cumulative mass profile.

Fig. 4 shows the inverse magnification results. For each case, the smoothing was fixed to the same value over all the points calculated. The green circles, blue diamonds and red triangles are, respectively, for smoothing scales of 100, 1000 and 10 000 times smaller than the galaxy radius. From this, we clearly see that a variable smoothing scale would be desirable. In the outer roughly 2 arcsec, we see that the green point accurately follow the analytic predictions with minimal spread, whereas the red triangles suffer a substantial spread due to shot noise. However, in the inner regions, the green points are incapable of finding the critical curves, points where the inverse magnification is zero; hence, we would not recognize this as a system capable of having multiple images. With the blue points, we are able to accurately find the tangential critical curve ($\sim$1 arcsec), with very little spread, but fail to capture the radial critical curve ($\sim$0.15 arcsec). In these very inner regions, the red points do better but the spread is still substantial.

From now on, we consider the case where an adaptive smoothing is set following the procedure described in Section 2.3.3. Unless specified otherwise, we set $N_\sigma = 256$. Fig. 5 shows the deflection angle calculation for the same halo as in Fig. 4. As expected we see that the deflection angle is easily calculated for a wide range of projected radii. A close inspection shows that angles are slightly underestimated with $N_\sigma = 256$, while reducing the smoothing to $N_\sigma = 64$ puts the computed points closer to the theoretical curve. The discrepancy between the theory and the calculation is

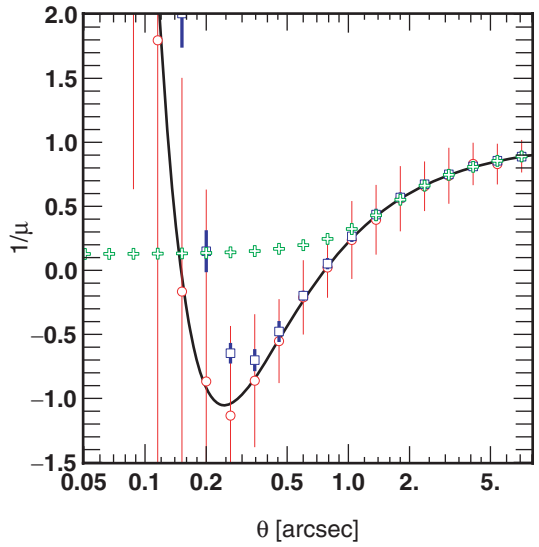

Figure 4. The inverse magnification of an NSIS with a core radius of 0.037 arcsec ($r_h/2000$). The solid line shows the analytic solutions. The points are the results of SPL calculations on a distribution with 10^7 particles. In each case, a constant smoothing scale is used; the circles (red) are for a smoothing of $\sigma = 0.0074$ arcsec, the squares (blue) are for $\sigma = 0.074$ arcsec and the crosses (green) are for $\sigma = 0.74$ arcsec.

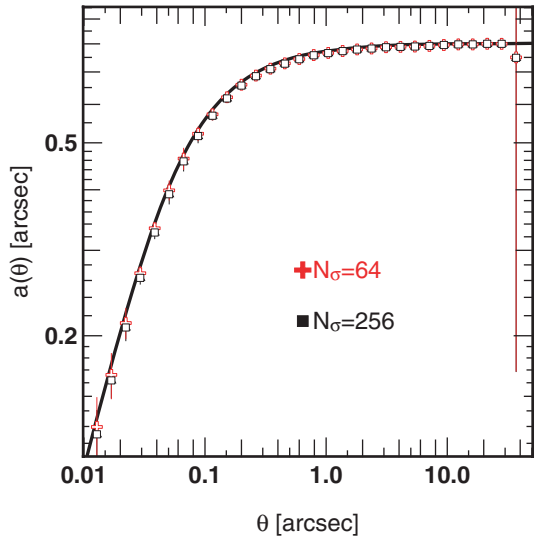

Figure 5. The deflection angle of an NSIS with a core radius of 0.037 arcsec ($r_h/2000$). The solid black line is the analytic solution and the symbols are those measured using the SPL method with adaptive smoothing. Computations for $N_\sigma = 64$ (red crosses) and $N_\sigma = 256$ (black squares) are shown. The bars stand for 3σ dispersion.

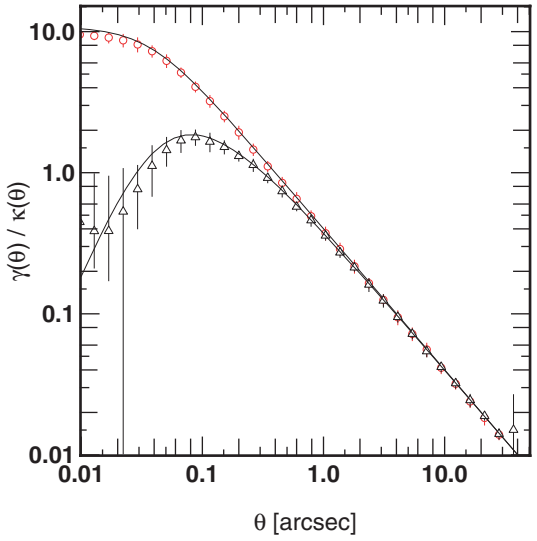

Figure 6. The solid black line shows the analytic solution for the convergence κ of the NSIS with a core radius of 0.037 arcsec ($r_h/2000$) and the dashed line shows the magnitude of the shear ($|\gamma|$). Overplotted are the convergence (red circle) and the absolute shear (black triangles) calculated using the SPL method on a distribution containing 10^7 particles using adaptive smoothing ($N_\sigma = 256$). The bars stand for 3σ dispersion.

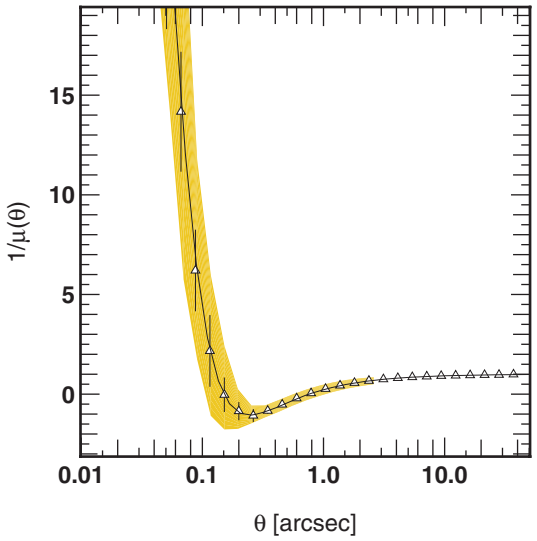

Figure 7. The inverse magnification of the NSIS with a radius of 0.037 arcsec ($r_h/2000$). The solid black curve shows the analytic solution. The shaded areas stand for the results of an FFT calculation performed on a 4096×4096 grid on a distribution made up of 10^7 particles. The extension of the shaded area shows the 3σ dispersion of the FFT calculation. The triangles show the SPL measurements on the same distribution using adaptive smoothing ($N_\sigma = 256$). The bars stand for the 3σ dispersion.

$\sim$2 per cent for $N_\sigma = 256$ and $\sim$1 per cent for $N_\sigma = 64$ (see also Fig. 10). This suggests that the discrepancy is due to oversmoothing. We also recall that the mass profile is reproduced at a 1 per cent level or better (see Fig. 3): this 2 per cent deviation in the angle profile is then unlikely to be related to the sampling of the halo by particles. We comment further this oversmoothing effect in Section 3.1.3.

In Fig. 6, we clearly see that the convergence and the shear fields are more sensitive to shot noise than the deflection angles, but the overall theoretical trend is qualitatively reproduced. Finally, these are combined to calculate the inverse magnification shown in Fig. 7. Here both the results from the SPL method (points with the error bars) and the FFT method (shaded area) are shown. Clearly, SPL does as well as the grid-based method and even exhibits a smaller scatter than the FFT+CIC computation. Let us emphasize that the scatter induced by the FFT may be reduced by the use of other smoothing kernels for instance, but it is beyond the scope of the current paper to perform an extensive comparison of grid-based methods. We also recall that SPL allows to sample the field at points

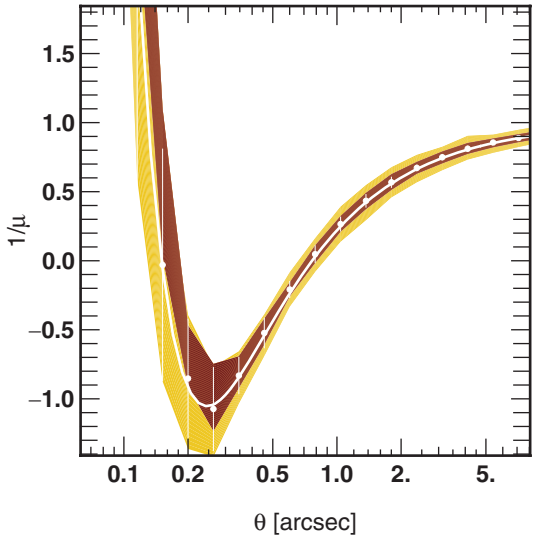

Figure 8. The inverse magnification computed with a constant smoothing length (shaded areas) and with an adaptive smoothing strategy (markers with the error bars). The dark (light) shaded area has a constant smoothing length equal to the adaptive smoothing length derived at the inner (outer) critical curve location. The white curve stands for the theoretical inverse magnification profile.

of interest to us, in this particular case using concentric rings in order to investigate the impact of smoothing as a function of radius. Meanwhile for the FFT, the number of points located at a *constant* radius is reduced to a few because of the grid sampling. For this reason, the shaded area in Fig. 7 represents the extent of the FFT computation's cloud and not the real scatter measured at a given radius. Therefore, the only way to increase the number of points at a given radius is to increase the resolution, a consuming strategy in terms of, for example, memory, while for the SPL this increase is easily performed. Finally, the comparison of Fig. 7 to Fig. 4 makes clearly the case in favour of an adaptive smoothing strategy for a better control of the spread induced by the Poisson noise.

In order to emphasize the requirement of an adaptive smoothing, we present in Fig. 8 a comparison of the previous adaptive calculation of the inverse magnification to two constant-smoothing calculations: the σ_S were chosen to coincide with the two adaptive smoothing lengths measured at the zeros of the function ($\sigma = 0.017$ and 0.037 arcsec). Even though the smoothings only differ by a factor of 2.2, no satisfying result could be found on the whole range of radii investigated using adaptive SPL. The smallest smoothing (light shaded area in the figure) induces a large spread for $\theta > 0.5$ arcsec, while the large smoothing strategy (dark shaded area) fails to reproduce the inner critical curve. Furthermore, the scatter at large radii for the latter case shows no improvement compared to the adaptive calculation. At best, a constant smoothing strategy would require a very fine tuning of the smoothing length, which should clearly be avoided.

Finally, we show in Fig. 9 the same calculations performed on the same model but sampled using only 10^6 particles. We applied an adaptive smoothing with $N_\sigma = 32$, 64, 128 and 256. The deflection angles are accurately computed, even though large smoothing values seem to slightly affect the calculation close to the halo's centre. On the other hand, the inverse magnification is clearly more sensitive to the lower resolution of this halo, especially close to the centre. A large smoothing value leads to a limited spread but the inner rise

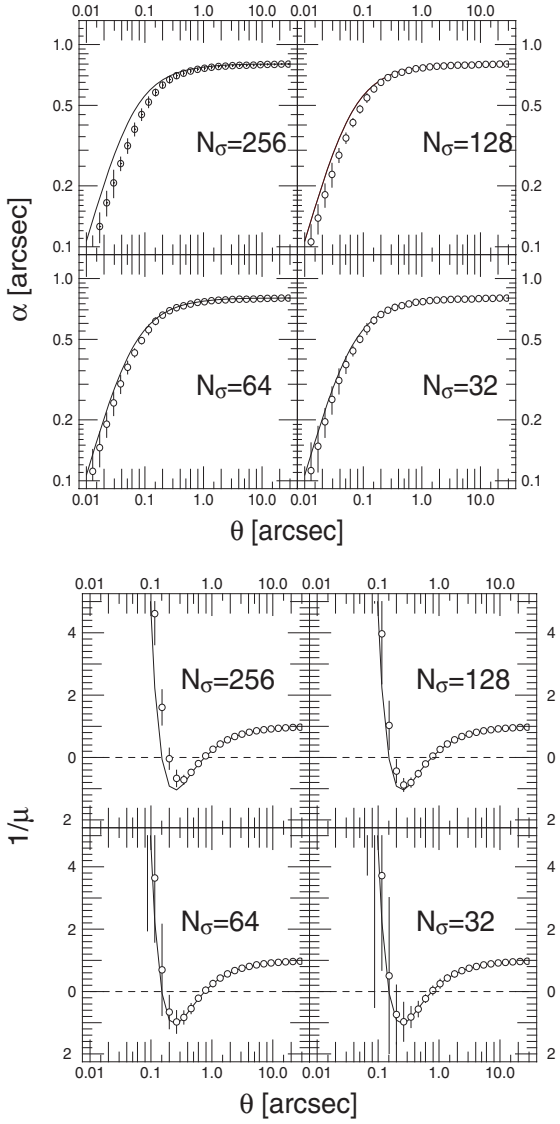

Figure 9. Deflection angle (top panel) and inverse magnification (bottom panel) of the NSIS with a core radius of 0.037 arcsec (r_h/2000). The model is sampled with 10^6 particles. The SPL calculation is performed with $N_\sigma =$ 256, 128, 64 and 32. The solid lines stand for the analytic profiles.

of the inverse magnification is incorrectly reproduced and occurs at larger radii than in the analytic solution. Conversely, a small smoothing value seems to provide a better fit to the analytic magnification profile in these innermost regions, but the spread becomes very important. Consequently, constraints on the radial caustic would be highly uncertain even though they would be closer on average to the prediction. We conclude that such a halo is not suited to study the lensing properties of such models via SPL and we argue that it is very unlikely that another method would be able to compute correctly the lensing signal of the underlying model. Consequently, the limitation is clearly induced by the halo (or the *N*-body simulation) and not by an inability to compute the signal properly.

3.1.3 Opening angle

Let us now investigate the influence of the opening angle involved on the SPL calculations. Fig. 10 shows the error on SPL calculations

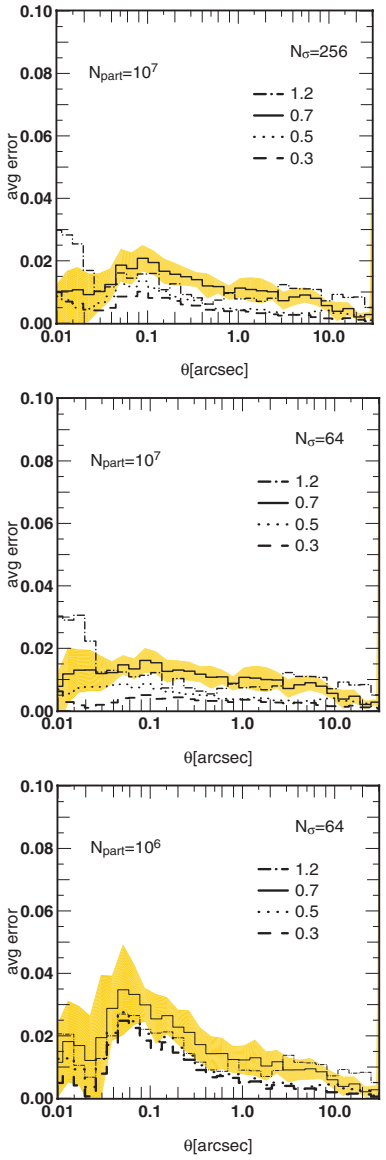

Figure 10. Relative error on the deflection angle profile for an NSIS model sampled with 10^7 particles (top and middle panels) and 10^6 (bottom panel). At each radius, the average error (over 32 points) relative to the direct computation ($\theta_{\rm Tree} = 0$) is shown for $\theta_{\rm Tree} = 0.3,\ \ 0.5,\ \ 0.7$ and 1.2 and for $N_\sigma = 256,\ \ 64$ and 64. The shaded areas represent the 1σ dispersion.

of the α profile for different opening angles and different N_σ. Computations were performed on the NSIS model with 10^7 particles. Errors were computed by comparison with the direct force calculation (corresponding to $\theta_{\rm Tree} = 0$) : all the particles' contributions were directly used to compute the angles without relying on a description in terms of distant macroparticles. Only the average error within a radial bin is shown in Fig. 10 while the dispersion is $\sim$1 per cent.

For $\theta_{\rm Tree} < 1.2$, the error remains typically below a few per cent for $N_\sigma = 64$, 128 and 256. As expected, the error decreases with $\theta_{\rm Tree}$, being smaller than the per cent. For $\theta_{\rm Tree} < 0.5$. Our cardinal choice ($\theta_{\rm Tree} = 0.7$) leads to errors lying between 1 and 2 per cent with an average of 1.5 per cent. Moreover, the relative error peaks around $\theta = 0.1$ arcsec: it corresponds to a region where the approximation of a configuration of particles within cells by a distant macroparticle is less valid. This effect relates to the oversmoothing observed in Section 3.1.2. Force in the outer regions is dominated by distant particles (in the inner regions) which are well represented by distant macroparticles. Meanwhile, inner regions are dominated by close particles which are correctly treated as single particles (i.e. fully-opened cells) because of the high density, even for large values of $\theta_{\rm Tree}$. Therefore, the intermediate regions, where none of the two previous regimes dominates, present the larger error. This error increases with N_σ because it increases the apparent size of the macroparticles, and thus their large distance influence on the α calculation. The same test is performed with the 10^6 simulation and $N_\sigma = 64$. We recall that for a given N_σ the actual size of the smoothing kernel is $10^{2/3}$, approximately five times bigger than that for a halo with 10^7 particles: these measures should, in principle, be compared to an $N_\sigma = 300$–10^7 result. The errors achieve a level of 3–3.5 per cent and given the dispersion, they depend only weakly on the opening angle. Clearly, oversmoothing of macroparticles dominates in this situation. It confirms that $N_\sigma = 32$ would be preferable for the computation of deflection angle, knowing that it would induce a strong scatter in the computation of second-derivative quantities (γ, κ and μ).

The value of $\theta_{\rm Tree} = 0.7$ is commonly used in tree-based computations. Clearly, better results could be obtained with smaller opening angles, but it led to satisfying results at the current test stage, especially regarding 2D maps (see the next section) and caustic/critical line locations. However, the errors' dispersion does not allow us to clearly distinguish the quality of the results obtained with one opening angle from another. At the current stage, the smoothing parameter seems to be more crucial to set the computations' level of accuracy. Future studies that require strong quantitative constraints must establish if such an accuracy is sufficient and if a smaller $\theta_{\rm Tree}$ must be used or not. Finally, we recall that no quadrupole expansion has been used in the current calculations: the future inclusion of higher-order corrections in the particle distribution within cells will clearly improve the accuracy of the computation for a given choice of opening angle.

3.1.4 Magnification maps

The radial properties of the lensing fields discussed thus far give insight into the strengths of each method. It is also very important to look at the lensing field in 2D. Fig. 11 shows the inverse magnification for four difference cases. Panel (a) shows the results of the highest-resolution FFT grid calculation that we were able to perform (4096 × 4096). The pixel scale on this zoom in is clearly visible since the image is made up of $\sim$160 × 160 pixel. Although it may be possible to optimize our routines further, it is not likely that we will be able to increase the resolution by more than a factor of 2. Panel (b) of Fig. 11 shows a set of SPL calculations performed at the same grid points as the FFT results of panel (a) and with a fixed smoothing scale that is comparable to the CIC smoothing. These two 'low-resolution' results are in good agreement with each other. However, since the SPL calculations were performed only on the points shown, the SPL method was faster. Panel (c) shows SPL results where the inverse magnification is sampled with 1024 × 1024 points on a polar grid with a fixed smoothing scale of 10^{-4} in units of the virial radius. Here, the features from panels (a) and (b) can been seen in detail and since they are persistent throughout all the calculations, we must conclude that the 'flame' patterns are indeed real features unique to this realization of the halo. They are the result of shot noise due to finite mass resolution. Panel (d) shows the image of the inverse magnification when using adaptive

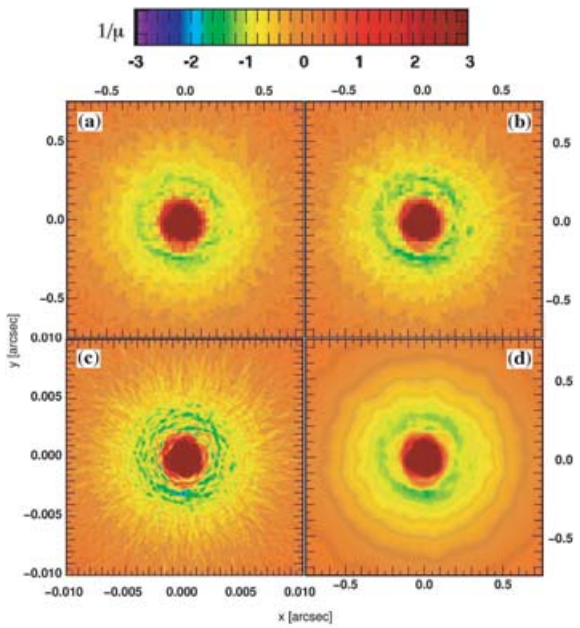

Figure 11. The inverse magnification for the NSIS. Panel (a) shows the results from the FFT calculation on 4096^2. Panel (b) shows the result from the SPL calculation with a smoothing scale comparable to the CIC smoothing scale of the FFT calculation with sampling at the same grid points as the FFT calculation. Panel (c) shows the inverse magnification using the SPL routine where the number of points is increased to 1024×1024 pixels and the smoothing scale is set to a constant 10^{-4}. In this panel, coordinates are given in units of the virial radius. The sampling used in panel (d) is the same as used in panel (c); however, in panel (d) an adaptive smoothing scale that is linked to underlying surface density is used.

smoothing with $N_\sigma = 256$. We see that by doing this we have managed to greatly reduce the 'flame' features, although the pattern is not perfectly symmetric as would be the case with infinite mass resolution.

3.1.5 Critical and caustic curves

The final remaining features of the NSIS are the critical and caustic curves. These are shown in Fig. 12. Here, the solid curves are the caustics and the dashed curves are the critical curves. Shown in red are the curves we measure using our SPL method and in black are the analytic solutions for our NSIS. Clearly, the two results agree very well and provide a 2D validation of the whole technique.

The location of SPL's critical curves also permits us to investigate the halo's mass-resolution issues. In Fig. 13, we show the critical lines computed for two haloes with 10^6 and 10^7 particles and for two different smoothing ($N_\sigma = 32$ and 256). Considering the 10^7 halo first, increasing N_σ removes the small-scale features in the magnification map and reduces the spread around the analytic solution, the critical curves. In general, the overall structure of these lines is well reproduced in all the cases. For the 10^6-particle halo, the same behaviour occurs for the outer critical curve: more smoothing gives reduced spread and a better agreement with the analytic solution. However, the inner curve drifts outwards from the correct location as N_σ increases, even though the spread is reduced. Clearly, no good compromise can be found between resolution and noise control for a halo with this lower mass resolution.

We stress again that no grid-based interpolation has been used here to compute the deflection angle on the critical lines and map them back to caustics. A first computation has been performed to spot the critical lines [using the same procedure which results in panel (d) in Fig. 11]. The exact deflection angles were then computed along these critical lines only.

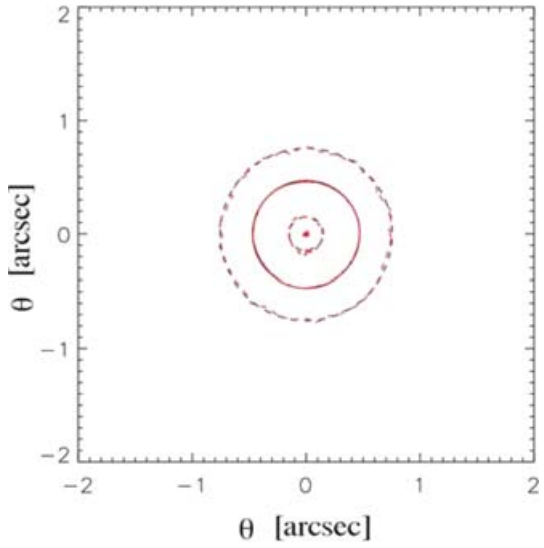

Figure 12. The critical and caustic curves for the NSIS. The dashed red lines are the critical curves; the solid red lines are the corresponding caustics. The black curves are the analytic solutions and the red lines are the results for SPL on a distribution with 10^7 particles and core radius of 0.037 arcsec (r_h/2000).

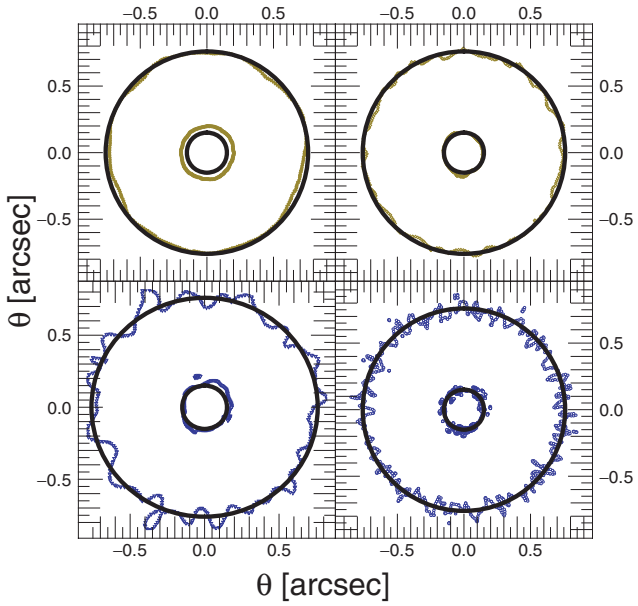

Figure 13. Critical curve locations for our template NSIS sampled with 10^6 (left-hand column) and 10^7 (right-hand column) particles. SPL calculations are performed with $N_\sigma = 32$ and 256 (respectively, bottom and top rows) on a 256×256 logarithmically sampled polar grid. The dashed lines stand for the analytically derived locations of the critical curves. The solid lines stand for the SPL calculations.

3.2 Non-Singular Isothermal Ellipsoid

We continue our investigation of the SPL technique by breaking the spherical symmetry. We computed the magnification maps and the deflection angles for the Non-Singular Isothermal Ellipsoids (hereafter NSIEs) described by Kormann, Schneider & Bartelmann (1994). These models are defined by the following projected density:

$$\kappa(\theta_x, \theta_y) = \frac{s_c\sqrt{e}}{2\sqrt{\theta_b^2 + \theta_c^2}}, \tag{23}$$

where the scaling s_c has been added to allow us to choose halo-mass configurations. We have selected models with a halo of mass $M_h = 1 \times 10^{13}\,M_\odot$ with a main axis' length $r_h = 0.5$ Mpc. The lens configuration is the same as the one chosen for the NSIS, that is, sources at $z = 3$ and a lens at $z = .8$. Besides the total mass and core radius, an additional parameter e, the axis ratio, introduces ellipticity into the model through:

$$\theta_b = \sqrt{\theta_x^2 + e^2\theta_y^2}, \tag{24}$$

where θ_x and θ_y are the directions in the x–y plane. We generated three 10^7 particles' models with $e = 0.2$, 0.4. and 0.8, and Fig. 14 shows the critical and caustic curve locations on the lens plane. SPL computations were performed with $N_\sigma = 128$ on a 256×256 logarithmic polar grid with $10^{-4} < r/r_h < 5 \times 10^{-2}$. Because the spherical symmetry is broken, the radial caustic is not degenerate anymore: it allows us to probe the accuracy of the outer critical curve's computation in a regime where the projected density is lower than that in the central regions. Clearly, the match between SPL calculations (shown in red) and the analytic solution (shown in black) is good and the lines are almost indistinguishable. Realistic dark matter haloes exhibit a certain level of triaxiality which should be easily handled with the current technique. In particular, 'naked cusps' (i.e. cusps outside the radial caustics) are accurately reproduced, even for the most-flattened models. Therefore, image multiplicity statistics, the relative numbers of two- and four-image regions and naked cusp systems, should be well reproduced by the simulations.

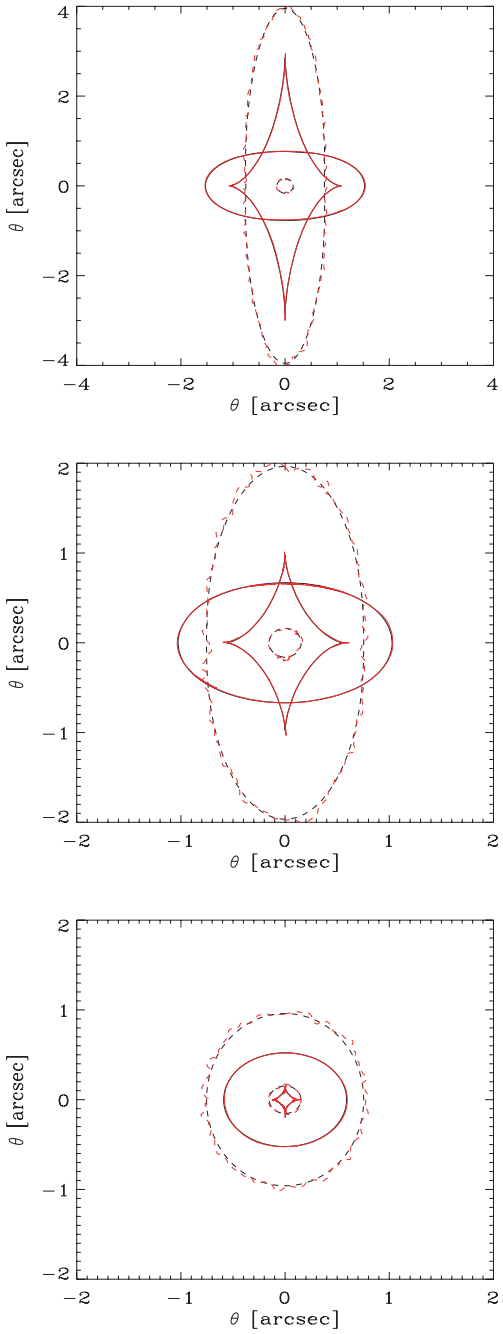

Figure 14. Critical (dashed) and caustic (plain) curves for the three different NSIE models: $e = 0.2$, 0.4 and 0.8 (from top to bottom panel). SPL calculations (red online) are compared to analytic solutions (black online). NSIE models are sampled with 10^7 particles and $M_h = 10^{13}\,M_\odot$ and a core radius, $r_c = r_h/2000$ with $r_h = 500$ kpc. SPL calculations were performed with $N_\sigma = 128$ on a 256×256 polar grid.

4 SUMMARY AND PROSPECTS

We present a method for computing the gravitational lensing induced by simulated gravitational lenses. It solves the Poisson equation using a 2D-Tree decomposition technique combined with a description of simulation particles as 'extended clouds'. The so-called 'SPL' technique allows the *direct* computation of any linear operation on the deflection potential, such as the derivatives involved in deflections angles, convergence, and shear. We test this method using analytic models of NSIS and ellipsoids (NSIE). The lensing properties are very accurately reproduced if the mass resolution is high enough. For instance, the caustic structures, including naked cusps, are correctly reproduced even for highly flattened systems and therefore accurate predictions of the image multiplicities are expected.

These tests showed that adaptive smoothing is *necessary* if one wants to probe the whole lens plane to sufficient accuracy: a small smoothing scale does well in high-density regions but induces a large scatter in low-density environments. Conversely, overextended particles smooth over small-scale features, such as the inner cusp and substructures. In trying to achieve a compromise between smoothing and resolution, we found that the number of particles in simulated haloes can be critical to locating the critical and caustic curves. For instance, an NSIS with a 'core' as small as $r_h/2000$ and sampled with 10^6 particles cannot be fully investigated in our fiducial lens configuration ($z_l = 0.8$ and $z_s = 3.$). This emphasizes the need of high-resolution haloes in order to accurately predict the strong lensing produced by these objects.

Because it combines noise-control with high resolution, this tool is particularly suited to the study of the effect of substructures in dark matter haloes, topics such as violations of the cusp caustic relation between image magnifications or predictions of image multiplicities

(see e.g. Bradač et al. 2004; Amara et al. 2006). Because it does not suffer from periodic boundary conditions, SPL is naturally extended to weak-lensing studies of isolated objects such as galaxy clusters. In a large simulation box, the method will adapt to put computational power where it is most needed, improving the accuracy of shear correlations over a large range of scales (from clusters to degree-scale cosmic shear surveys) while reducing CPU time. Since a significant fraction of the *N*-body codes are based on tree structures, one could even imagine on-the-fly lensing calculations during the dynamical integration. A level of accuracy is achieved in our implementation of SPL where the calculation is effectively limited by the accuracy of the simulation used to find the mass distribution rather than the lensing code itself.

ACKNOWLEDGMENTS

We are grateful to E. Audit, R. Teyssier and A. Refregier for useful comments and helpful suggestions. DA acknowledges support from the *HORIZON* project (www.projet-horizon.fr) and AA was supported as part of the *Dark Universe Explorer* (*DUNE*).

REFERENCES

Amara A., Metcalf R. B., Cox T. J., Ostriker J. P., 2006, MNRAS, 367, 276
Bahcall N. A., Ostriker J. P., Perlmutter S., Steinhardt P. J., 1999, Sci, 284, 1481
Barnes J., Hut P., 1986, Nat, 324, 446
Bertschinger E., 1998, ARA&A, 36, 599
Bode P., Ostriker J. P., 2003, ApJS, 145, 1
Bouchet F. R., Hernquist L., 1988, ApJS, 68, 521
Bradac M., Schneider P., Steinmetz M., Lombardi M., King L. J., Porcas R., 2002, A&A, 388, 373
Bradač M., Schneider P., Lombardi M., Steinmetz M., Koopmans L. V. E., Navarro J. F., 2004, A&A, 423, 797
Chiba M., 2002, ApJ, 565, 17
Dalal N., Kochanek C. S., 2002, ApJ, 572, 25
Dikaiakos M., Stadel J., 1996, Proc. 10th ACM Intl. Conf., Supercomputing, ACM Press, New York, p. 94
Evrard A. E., Virgo Collaboration, 1999, BAAS, 31, 917
Kazantzidis S., Mayer L., Mastropietro C., Diemand J., Stadel J., Moore B., 2004, ApJ, 608, 663
Klypin A., Kravtsov A. V., Valenzuela O., Prada F., 1999, ApJ, 522, 82
Kormann R., Schneider P., Bartelmann M., 1994, A&A, 284, 285
Li G., Mao S., Jing Y., Kang X., Bartelmann M., 2006, ApJ, 652, 43
Mao S., Jing Y., Ostriker J. P., Weller J., 2004, ApJ, 604, L5
Mao S., Schneider P., 1998, MNRAS, 295, 587
Meneghetti M., Bolzonella M., Bartelmann M., Moscardini L., Tormen G., 2000, MNRAS, 314, 338
Metcalf R. B., Madau P., 2001, ApJ, 563, 9
Metcalf R. B., Zhao H., 2002, ApJ, 567, L5
Metcalf R. B., Moustakas L. A., Bunker A. J., Parry I. R., 2004, ApJ, 607, 43
Moore A., 1991, PhD thesis, Univ. Cambridge
Moore B., Ghigna S., Governato F., Lake G., Quinn T., Stadel J., Tozzi P., 1999, ApJ, 524, L19
Moore B., Governato F., Quinn T., Stadel J., Lake G., 1998, ApJ, 499, L5
Moustakas L. A., Metcalf R. B., 2003, MNRAS, 339, 607
Navarro J. F., Frenk C. S., White S. D. M., 1995, MNRAS, 275, 56
Navarro J. F., Frenk C. S., White S. D. M., 1996, ApJ, 462, 563
Navarro J. F., Steinmetz M., 1997, ApJ, 478, 13
Puchwein E., Bartelmann M., Dolag K., Meneghetti M., 2005, A&A, 442, 405
Smith R. E. et al., 2003, MNRAS, 341, 1311
Spergel D. N. et al., 2003, ApJS, 148, 175
Stoehr F., White S. D. M., Tormen G., Springel V., 2002, MNRAS, 335, L84
Van Waerbeke L., Mellier Y., 2003, online-only reference: astro-ph/0305089
Wambsganss J., Cen R., Ostriker J. P., 1998, ApJ, 494, 29
Wang L., Caldwell R. R., Ostriker J. P., Steinhardt P. J., 2000, ApJ, 530, 17
Weller J., Ostriker J. P., Bode P., Shaw L., 2005, MNRAS, 364, 823

This paper has been typeset from a TEX/LATEX file prepared by the author.